The puzzling X-ray continuum of the quasar MR 2251−178

E. Nardini,, N. Reeves, J., Delphine Porquet, V. Braito,, N. Grosso,, J. Gofford,

Mon. Not. R. Astron. Soc. **000**, 1–14 (2014) Printed 14 August 2021 (MN LATEX style file v2.2)

The puzzling X-ray continuum of the quasar MR 2251−178

E. Nardini,[1⋆] J. N. Reeves,[1,2] D. Porquet,[3] V. Braito,[4] N. Grosso,[3] J. Gofford[1]
[1] *Astrophysics Group, School of Physical and Geographical Sciences, Keele University, Keele, Staffordshire ST5 5BG, UK*
[2] *Department of Physics, University of Maryland Baltimore County, 1000 Hilltop Circle, Baltimore, MD 21250, USA*
[3] *Observatoire Astronomique de Strasbourg, CNRS, UMR 7550, 11 rue de l'Université, 67000 Strasbourg, France*
[4] *INAF – Osservatorio Astronomico di Brera, via E. Bianchi 46, 23807 Merate, Italy*

Released Xxxx Xxxxx XX

ABSTRACT

We report on a comprehensive X-ray spectral analysis of the nearby radio-quiet quasar MR 2251−178, based on the long-look ($\sim$ 400 ks) *XMM–Newton* observation carried out in November 2011. As the properties of the multiphase warm absorber (thoroughly discussed in a recent, complementary work) hint at a steep photoionizing continuum, here we investigate into the nature of the intrinsic X-ray emission of MR 2251−178 by testing several physical models. The apparent 2–10 keV flatness as well as the subtle broadband curvature can be ascribed to partial covering of the X-ray source by a cold, clumpy absorption system with column densities ranging from a fraction to several $\times 10^{23}$ cm^{-2}. As opposed to more complex configurations, only one cloud is required along the line of sight in the presence of a soft X-ray excess, possibly arising as Comptonized disc emission in the accretion disc atmosphere. On statistical grounds, even reflection with standard efficiency off the surface of the inner disc cannot be ruled out, although this tentatively overpredicts the observed $\sim$ 14–150 keV emission. It is thus possible that each of the examined physical processes is relevant to a certain degree, and hence only a combination of high-quality, simultaneous broadband spectral coverage and multi-epoch monitoring of X-ray spectral variability could help disentangling the different contributions. Yet, regardless of the model adopted, we infer for MR 2251−178 a bolometric luminosity of $\sim$ 5–7 $\times$ 10^{45} erg s^{-1}, implying that the central black hole is accreting at $\sim$ 15–25 per cent of the Eddington limit.

Key words: Galaxies: active – X-rays: galaxies – Quasars: individual: MR 2251−178

1 INTRODUCTION

Among the X-ray brightest Active Galactic Nuclei (AGN) in the local Universe due to its 2–10 keV luminosity largely exceeding 10^{44} erg s^{-1}, MR 2251−178 ($z \simeq 0.064$; Canizares, McClintock & Ricker 1978) is a spectacular object in every respect. It was the first quasar to be detected and identified through X-ray observations (Cooke et al. 1978; Ricker et al. 1978), as well as the first one where the presence was established of *warm* absorption by photoionized gas, variable in both ionization state and possibly column density over timescales of less than one year (Halpern 1984). The source was later found to experience appreciable changes in the X-ray flux over periods of $\sim$ 10 days (Pan, Stewart & Pounds 1990), with a tight correlation between the ionization parameter of the absorbing gas[1] and the continuum luminosity (Mineo & Stewart 1993). Narrow absorption lines with a systematic blueshift of $\sim$ 300 km s^{-1} have been detected in the ultraviolet (UV) due to Lyα, N v and C iv (Monier et al. 2001). In particular, the C iv doublet apparently vanished in less than four years (Ganguly, Charlton & Eracleous 2001), implying that the UV absorber is truly local to the AGN, and that it is possibly one and the same with the soft X-ray warm absorber. Much deeper insights came with the advent of high-resolution X-ray spectroscopy. Early *XMM–Newton* Reflection Grating Spectrometer (RGS) observations hinted at a multiphase configuration for the warm absorber, likely consisting of two or three distinct components (Kaspi et al. 2004), while the *Chandra* High Energy Transmission Grating (HETG) spectrum revealed a highly ionized absorption feature in the iron K band, interpreted as the Fe xxvi Lyα line at the sizable outflow velocity of $v_{\rm out} \sim 0.04c$ (Gibson et al. 2005). The corresponding mass-loss rate was calculated to be at least an order of magnitude larger than the accre-

⋆ E-mail: e.nardini@keele.ac.uk

[1] The ionization parameter is defined as $\xi = L_{\rm ion}/nr^2$, where n is the electron density of the gas and r is its distance from an ionizing source with 1–1000 Ry luminosity $L_{\rm ion}$ (Tarter, Tucker & Salpeter 1969).

tion rate, unless the covering fraction of the outflow is very small.

The environment of MR 2251−178 is likewise exceptional. The quasar lies in the outskirts of a loose, irregular cluster with several tens of galaxies (Phillips 1980), and is surrounded by a huge emission-line nebula detected in Hα and [O III] at optical wavelengths out to a distance of ~ 100 kpc from the central source (Bergeron et al. 1983; Shopbell, Veilleux & Bland-Hawthorn 1999). The knotty and filamentary appearance of this gaseous envelope is more typical of powerful radio galaxies, yet MR 2251−178 only shows weak radio emission, whose elongated morphology resembles a double-lobed jet-like structure (Macchetto et al. 1990). A similar spatial extent and orientation marks the ionization cones recently found through deep [O III]λ5007/Hβ and [N II]λ6583/Hα flux ratio maps (Kreimeyer & Veilleux 2013). Overall, the quasar radiation field can easily account for the ionization state of the nebula, which is arguably the most extended around a radio-quiet source. Its origin, however, is still unclear. Diffuse X-ray emission along some directions was preliminary reported by Gibson et al. (2005) based on the smoothed HETG zeroth-order image taken in 2002. Unfortunately, we cannot safely corroborate these findings through the much deeper 2011 HETG data set, since the artificial broadening of the instrumental Point Spread Function due to photon pile-up overrides any faint contribution from the halo.[2]

Due to its key role as the underlying source of ionizing photons for the ambient gas, from nuclear to intergalactic scales, a proper knowledge of the shape and behaviour of the intrinsic X-ray continuum is highly desirable, yet most of the effort in the wealth of X-ray analyses performed so far has concentrated on improving the characterization of the multi-component warm absorber. Incidentally, all the X-ray spectral studies actually agree with describing the absorbed continuum by means of a power law of photon index $\Gamma \sim 1.6$, with a high-energy exponential cutoff at ~ 100 keV (Orr et al. 2001) and a soft excess below ~ 1 keV (Kaspi et al. 2004). In a recent paper, we have taken advantage of coordinated ~ 400+400 ks long *Chandra* HETG and *XMM–Newton* RGS observations to bring our grasp on the properties of the intervening ionized gas to unprecedented detail and energy resolution (Reeves et al. 2013; hereafter R13). Both campaigns were conducted as large programs in late 2011, with just a few weeks of separation from one another, and yielded intriguing information on the illuminating continuum itself, which below 2 keV is required to be much steeper ($\Gamma > 2$) than typically estimated at hard X-rays. Indeed, the analysis of the *Suzaku* spectrum carried out by Gofford et al. (2011) had already suggested that the broadband X-ray emission of MR 2251−178 can be reproduced equally well through a softer power law with $\Gamma \simeq 2$, provided that an additional cold-gas column of $N_{\rm H} \sim 10^{23}$ cm^{-2} covering a moderate fraction of the source is introduced.

In the wake of these indications, here we present a thorough investigation of the 0.3–10 keV EPIC/pn spectrum obtained in the 2011 *XMM–Newton* observation, with the aim of understanding the nature of the primary photoionizing continuum and unveiling the high-energy physical processes at work in the very central regions of this powerful quasar. This work is organized as follows. In Section 2 we provide the basic details about the *XMM–Newton* large observing program on MR 2251−178, and describe the principal steps of our data reduction. Section 3 is dedicated to the spectral analysis, whose results and main implications are discussed in Section 4. Our conclusions are drawn in Section 5. Throughout this paper we have assumed $H_0 = 70$ km s^{-1} Mpc^{-1}, $\Omega_m = 0.27$ and $\Omega_\Lambda = 0.73$, in agreement with the latest values of the concordance cosmological parameters (Hinshaw et al. 2013).

2 OBSERVATIONS AND DATA REDUCTION

The long-look *XMM–Newton* monitoring of MR 2251−178 was performed in separate exposures over three consecutive satellite orbits, starting on 2011 November 11, 13, and 15, respectively (ObsIDs 0670120201–301–401; PI: J. Reeves). The corresponding data files were processed with the Science Analysis System (SAS) v12.0, and were inspected with the standard software packages. As the source is quite bright, all the EPIC cameras were operated in small window mode, in order to avoid the distortion effects of photon pile-up by virtue of the reduced frame time. According to the 10–12 keV light curves, no strong background flaring occurred during any of the observations; only a modest rise is seen at both the start and the end of the first and the third ones. These periods of weak background activity were rejected adopting a threshold of 0.5 counts s^{-1} for the pn, and of 0.35 counts s^{-1} for the two MOS detectors. However, due to an average 0.3–10 keV count rate of ~ 4.3 s^{-1} over a 25″ extraction region, the MOS spectra turned out to be still moderately piled-up, and have not been used in this work.

The EPIC/pn spectra of the source were extracted from a circular region with radius of 36″ centred on the target, while the background was evaluated on two identical areas of smaller size (31″) at $\sim 3\farcm5$ of distance. The same extraction regions were used for all the data sets, in view of their possible merging in the absence of any significant spectral variability during the span of the entire campaign. Indeed, Fig. 1 shows the background-subtracted 0.3–10 keV light curve of MR 2251−178, along with seven narrow-band hardness ratios with respect to the 0.3–0.5 keV energy range. While the overall flux is slowly decreasing, there is no evidence of conspicuous changes in the spectral shape. This was also confirmed by the comparison of the three X-ray spectra averaged over the separate observations, which were therefore combined into a single one. Given the lower pn live time in small window mode (71 per cent), the total effective exposure is ~ 270 ks. Individual redistribution matrices and ancillary response files at the source position were created through the SAS tasks `rmfgen` and `arfgen`, and were subsequently merged as well. The X-ray data were grouped to a minimum of 200 counts per energy channel, and the spectral analysis was performed using the XSPEC v12.8 fitting package. All the uncertainties are quoted at the 90 per cent confidence level ($\Delta\chi^2 = 2.71$) for the single parameter of in-

[2] The AGN flux in the 2011 *Chandra* observation was larger by ~ 50 per cent with respect to 2002. While the effects of pile-up on the Point Spread Function can be qualitatively simulated, they prevent any accurate image reconstruction.

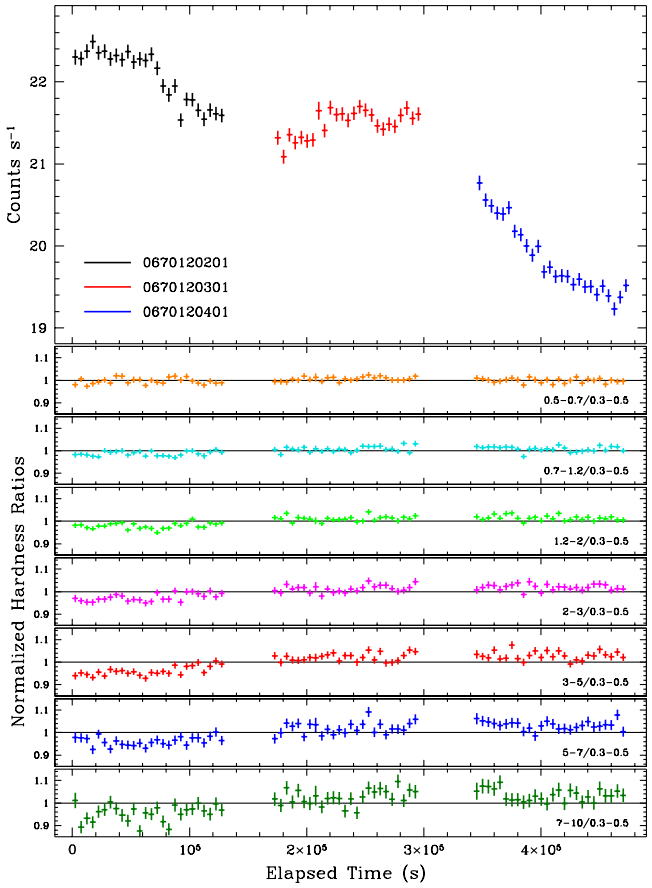

Figure 1. Top panel: light curve of MR 2251−178 in the 0.3–10 keV energy band after background subtraction and dead-time correction, plotted with a time bin of 5 ks. The peak-to-peak variation in the count rate is 15 per cent. Bottom panels, respectively from above: 0.5–0.7, 0.7–1.2, 1.2–2, 2–3, 3–5, 5–7, 7–10 over 0.3–0.5 keV hardness ratios, normalized to their best-fitting constant values to stress the limited extent of any spectral change.

terest, while line energies are given in the rest frame, unless otherwise stated.

We have also taken into account the target photometry in the six wide-band filters of the Optical Monitor (OM), whose data were reprocessed with the `omichain` pipeline. Only the small high-resolution window at the centre of the field of view has been considered. Count rates were averaged over the different exposures, with a 10 per cent uncertainty added in quadrature owing to possible systematics in the fluxes of the standard stars. An absorption correction was also applied, based on the foreground dust reddening maps of Schlegel, Finkbeiner & Davis (1998) and the extinction law of Cardelli, Clayton & Mathis (1989). With $E(B-V) = 0.0390(\pm0.0013)$, averaged within a $5'$ radius from MR 2251−178, and $R_V = A(V)/E(B-V) = 3.1$ as per the standard value for the diffuse interstellar medium, we obtain $A(V) = 0.121(\pm0.004)$ mag, which leads to a flux correction ranging from $\sim$ 1.12 (V band) to 1.42 (UVW2 band).

3 SPECTRAL ANALYSIS

Limited to the X-ray domain, there are still many questions regarding MR 2251−178. While further progress on the side of the warm absorber above 2 keV will perhaps be feasible only with the new technology of X-ray micro-calorimeters onboard the future *Astro–H* mission, at present the most critical point involves the origin and intrinsic properties of the continuum. The photon index observed in this source is unusually hard compared to the average value of $\Gamma \sim 1.9$ generally found among radio-quiet quasars in the same X-ray luminosity range (e.g. Piconcelli et al. 2005; Scott et al. 2011). Yet the intensity of the warm absorption lines entails a much softer radiation field below 2 keV ($\Gamma \sim 2.5$; R13), denoting either an intrinsically steep continuum (which could be missed if some fraction of it were intercepted by cold gas layers still left unmodelled) or an inherent soft excess (e.g. Done et al. 2012). After a brief overview of the main results from our recent high-resolution analysis, in this Section we explore in depth the partial covering conjecture and other possible interpretations for the broadband X-ray emission of MR 2251−178.

3.1 Review of RGS and HETG observations

As discussed in detail in R13, both the *XMM–Newton* RGS and the almost coeval *Chandra* HETG spectra reveal the presence of multiple, partially ionized gas components along the line of sight to the primary X-ray source in MR 2251−178. After a preliminary Gaussian fit of the individual lines for parameterization and identification purposes, the absorption spectra were modelled by means of self-consistent photoionization grids generated through the XSTAR code v2.2 (e.g. Kallman & Bautista 2001), and implemented within XSPEC as multiplicative tables. Three fully-covering warm absorption components were required in order to account for the wealth of atomic transitions and the wide ionization state of the gas. The generic spectral grid was computed assuming a power-law X-ray continuum with $\Gamma = 2$. The turbulence velocity was set to $\sigma_t = 100$ km s^{-1}, based on the narrow profile of most lines; larger values result in substantially worse fits. The electron density, instead, is not a highly sensitive parameter. The corresponding tables provide a good fit to the mid- to high-ionization lines, due to Fe L-shell ions as well as He- and H-like species of lighter elements like C, N, O, Ne, Mg and Si. A separate grid, finely tuned over a limited region of the parameter space and involving a steeper illuminating continuum ($\Gamma = 2.5$), was introduced to better match the intensity of the low-ionization inner-shell lines, including the Fe M-shell Unresolved Transition Array (UTA; e.g. Behar, Sako & Kahn 2001). Interestingly, this component seems to respond to long-term flux changes, thus being in photoionization equilibrium. The kinematics and variability properties indicate that warm absorption likely occurs beyond the pc scale, i.e. within the inner Narrow Line Region. Table 1 summarizes the specifics of each grid and the best-fitting values inferred from the RGS analysis (as per R13).

In the soft X-rays, both the RGS and HETG spectra are also characterized by a complex interplay between absorption and emission components, as several narrow absorption lines are found superimposed on broad emission features.

Table 1. Properties of the warm absorption grids and best-fitting parameters to the 2011 RGS spectra for a partial covering model. $\Gamma_{\rm pl}$: spectral index of the illuminating power law. n_e: electron density in cm^{-3}. $\sigma_{\rm t}$: turbulence velocity in km s^{-1}. $\mathcal{S}$: sampling points over the 0.1–20 keV energy range. $N_{\rm H}$: hydrogen column density in cm^{-2}. ξ: ionization parameter in erg cm s^{-1}. Δ: grid range. δ: grid step. $v_{\rm out}$: outflow velocity in km s^{-1}.

Component	(a)	(b)	(c)
$\Gamma_{\rm pl}$	2.5	2.0	2.0
$\log n_e$	10	10	10
$\sigma_{\rm t}$	100	100	100
$\log \mathcal{S}$	5.0	4.0	4.0
$\Delta \log N_{\rm H}$	20.7–21.7	18–24.5	18–24.5
$\delta N_{\rm H}$	1×10^{20}	0.5 dex	0.5 dex
$\log N_{\rm H,best}$	21.32	21.16	21.52
$\Delta \log \xi$	0–3	0–5	0–5
$\delta\xi$	0.2 dex	0.5 dex	0.5 dex
$\log \xi_{\rm best}$	1.27	2.02	2.78
$v_{\rm out}$	470	460	0

Table 2. Soft X-ray emission lines in the RGS spectra. E: rest energy in eV. F: photon flux in 10^{-5} cm^{-2} s^{-1}. EW: equivalent width in eV. σ_v: velocity width in 10^3 km s^{-1}.

ID	C VI	N VI	N VII	O VII	O VIII	Ne IX
E	362.8	418.5	498.8	564.5	654.6	905.1
F	35.8	5.9	10.1	38.4	6.5	1.2
EW	2.6	0.6	1.0	7.6	1.6	0.8
σ_v	4.5	1.5	0.4	4.4	1.3	0.1

Among the latter, the strongest and most statistically significant ($\Delta\chi^2 \simeq 390$ following its exclusion from the model) is detected around the rest-frame energy of 0.56–0.57 keV, as expected for the O VII triplet. If resolved into the resonance, intercombination and forbidden line, the intensity ratios and velocity width suggest an origin of such emission consistent with the Broad Line Region (BLR) scale. Conversely, some narrower profiles (like those of N VII Lyα and Ne IX) might arise at larger distances. The identification of all the soft X-ray emission lines and their main properties against a dual partial covering description of the underlying continuum (see below) are listed in Table 2. All these components were fitted with simple Gaussian profiles, and have been kept frozen in the present analysis whenever included in the models.

3.2 EPIC/pn spectral fitting

In agreement with all its previous observations, during the 2011 *XMM–Newton* long look the broadband X-ray emission of MR 2251−178 exhibits considerable spectral complexity. For the sake of illustration, Fig. 2 shows the ratio of the 0.3–10 keV EPIC/pn spectrum to a power law, assuming two different continuum bands (3–5 and 7–10 keV) as reference. The main components, as well as the overall curvature, are clearly brought out. At the same time, it is evident that both the depth of the warm absorption trough and the prominence of the contiguous soft excess strongly depend on the determination of the intrinsic continuum. To this aim, we have applied widely different physical models. In all our fits below, Galactic absorption has been modelled through the `tbabs` cross sections and solar abundances from Wilms, Allen & McCray (2000), with the hydrogen column density frozen to $N_{\rm H} = 2.4 \times 10^{20}$ cm^{-2} (Kalberla et al. 2005).

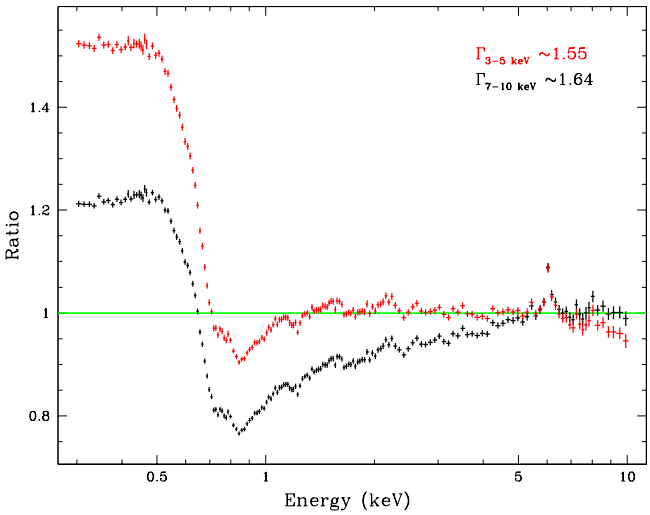

Figure 2. Data/model ratios obtained against the best-fitting power laws over the 3–5 (red) and 7–10 keV (black) bands, respectively. The X-ray spectral shape of MR 2251−178 is characterized by an apparent soft excess, a warm absorption trough, a narrow iron emission line, and a moderate curvature extending towards the higher energies. The determination of the intrinsic continuum is obviously critical to properly model all these observed features. (The data were rebinned for clarity).

3.2.1 Partial covering models

The sharp detection of tens of absorption lines in the high-resolution spectra amassed unique pieces of information on the primary photoionizing continuum, lending weight to a picture where the X-ray emission of MR 2251−178 is intrinsically much softer than previously thought. The warm absorber, however, has a minor effect on the observed slope (especially with its mid- and high-ionization layers), and also the global curvature is not fully accounted for. In order to achieve an adequate fit, a partially covering cold absorber was employed in the RGS analysis. Besides the superior statistics, this component has the advantage of naturally supplying a steeper photon index of $\Gamma \sim 2.3$, very close to the one dictated by the low-ionization lines. Reaching out to higher energies, the HETG spectrum accepts a second partial covering zone with higher column density to compensate for the residual curvature. Both components were reproduced through XSTAR grids. Due to the abrupt flattening below ~ 0.5 keV (e.g. Fig. 2), a modest amount (a few $\times10^{20}$ cm^{-2}) of neutral absorption local to the source was also included, possibly associated with the host galaxy rather than with the AGN environment.

With such a background, we have started our analysis of the 0.3–10 keV spectrum with the straight application of this benchmark model, which is dubbed as *pcovpow* hereafter for ease of discussion. Although the warm absorption parameters of Table 1 already provide a reasonable fit to the data

Table 3. Best-fitting parameters for the *pcovpow*, *discref* and *pcovref* physical models (see the text for details) in the 0.3–10 keV spectral range. Γ: power law photon index. K: power law normalization in 10^{-2} photons keV^{-1} cm^{-2} s^{-1} at 1 keV. $N_{\rm H}$: column density in cm^{-2}. ξ: ionization parameter in erg cm s^{-1}. f: covering fraction. $\Delta\chi^2$: variation in the fit statistics after removing a given component from the model and refitting. $Z_{\rm Fe}$: iron abundance in solar units. q: disc emissivity index for a power-law radial dependence, $\epsilon(r) \propto r^{-q}$. θ: disc inclination in degrees. $r_{\rm in}$: disc inner radius in $r_{\rm g}$. R: reflection strength. $F_{\rm obs}$: observed 0.3–10 keV flux in erg s^{-1} cm^{-2}. $L_{\rm int}$: intrinsic rest-frame 0.3–10 keV luminosity in erg s^{-1}. $\Delta\chi^2_{N_{\rm H},\xi}$: as above, but keeping the warm absorption $N_{\rm H}$ and ξ fixed to the best-fitting RGS values. (f): frozen parameter.

Model	*pcovpow*	*discref*	*pcovref*
	Power Law Continuum		
Γ	2.22±0.03	1.77±0.01	1.80±0.01
K	$4.06^{+0.27}_{-0.12}$	1.00±0.01	$1.07^{+0.03}_{-0.02}$
	Partial Covering (1)		
$\log N_{\rm H,1}$	22.78±0.02	–	$22.67^{+0.08}_{-0.11}$
$\log \xi_1$	$0.96^{+0.06}_{-0.08}$	–	0.0(f)
f_1	0.23±0.03	–	0.09±0.02
	Partial Covering (2)		
$\log N_{\rm H,2}$	23.82±0.02	–	–
$\log \xi_2$	$0.65^{+0.35}_{-0.17}$	–	–
f_2	$0.49^{+0.06}_{-0.04}$	–	–
$\Delta\chi^2$	358.9	–	–
	Disc Reflection		
$\log \xi_{\rm d}$	–	$0.80^{+0.01}_{-0.07}$	$0.80^{+0.01}_{-0.14}$
$Z_{\rm Fe}$	–	2.12±0.25	1.75±0.30
q	–	$3.0^{+2.7}_{-0.3}$	$4.4^{+2.8}_{-1.3}$
θ	–	24^{+3}_{-5}	24^{+2}_{-1}
$r_{\rm in}$	–	$5.2^{+4.3}_{-0.9}$	$9.0^{+3.2}_{-3.0}$
$R_{\rm d}$	–	$1.22^{+0.23}_{-0.19}$	$1.08^{+0.24}_{-0.36}$
$\Delta\chi^2$	–	987.1	420.7
	Remote Reflection		
$\log \xi_{\rm r}$	–	$2.49^{+0.02}_{-0.11}$	$2.17^{+0.04}_{-0.03}$
$R_{\rm r}$	–	$0.08^{+0.01}_{-0.02}$	0.07±0.01
$\Delta\chi^2$	–	127.1	108.0
	Warm Absorption (a)		
$\log N_{\rm H,a}$	21.25±0.04	21.10±0.05	$21.19^{+0.06}_{-0.08}$
$\log \xi_{\rm a}$	$1.23^{+0.11}_{-0.10}$	1.24±0.09	$1.26^{+0.06}_{-0.10}$
$\Delta\chi^2$	55.5	80.2	82.6
	Warm Absorption (b)		
$\log N_{\rm H,b}$	$21.49^{+0.07}_{-0.12}$	$22.80^{+0.11}_{-0.47}$	$21.20^{+0.13}_{-0.19}$
$\log \xi_{\rm b}$	$1.93^{+0.09}_{-0.04}$	$3.46^{+0.02}_{-0.04}$	$2.26^{+0.09}_{-0.07}$
$\Delta\chi^2$	41.5	20.8	18.0
	Warm Absorption (c)		
$\log N_{\rm H,c}$	$21.48^{+0.15}_{-0.11}$	21.56±0.04	$21.22^{+0.11}_{-0.20}$
$\log \xi_{\rm c}$	$2.79^{+0.08}_{-0.07}$	$1.86^{+0.04}_{-0.03}$	1.84±0.08
$\Delta\chi^2$	38.6	19.9	15.8
	General properties		
$\log N_{\rm H}(z)$	20.45±0.03	–	–
$\log F_{\rm obs}$	−10.19	−10.19	−10.19
$\log L_{\rm int}$	45.32	44.87	44.88
χ^2/ν	1887.3/1711	1899.5/1712	1857.7/1710
$\Delta\chi^2_{N_{\rm H},\xi}$	49.4	199.3	97.3

($\chi^2/\nu \sim 1937/1717$), the column densities and ionization states have been allowed to readjust to the broadband continuum. Only the outflow velocities were kept fixed, enabling a secure identification of each of the three original components. The improvement is significant but not dramatic, leading to $\chi^2/\nu \simeq 1887.3/1711$. In most cases the variation of $N_{\rm H}$ and ξ is minimal (see also Section 4), confirming that the warm absorber plays a little role in the 2–10 keV energy range. The power-law photon index $\Gamma \simeq 2.22$ lies in between the values inferred from the RGS and HETG, and also for the two partial covering components the agreement with the grating analysis appears to be excellent. The best-fitting parameters and the general properties of the *pcovpow* model are summarized in Table 3. No discrete detectable lines are connected with the partial covering absorbers, as implied by their small degree of ionization, $\log(\xi/{\rm erg\,cm\,s^{-1}}) \lesssim 1$. The major impact is clearly on the continuum. With a column density of $N_{\rm H,1} = 6.0(\pm0.3)\times10^{22}$ cm^{-2}, the first layer is responsible for an appreciable rollover below 2 keV (see Fig. 3). This explains why its presence is required in the RGS fit in spite of the narrow bandwidth. On the other hand, the evidence for an additional component is now compelling thanks to the much larger effective area of EPIC/pn with respect to HETG up to 10 keV. This supplementary screen with $N_{\rm H,2} = 6.6(\pm0.3)\times10^{23}$ cm^{-2} and covering fraction $f_2 \sim 0.5$ is in fact the main driver of the apparent flatness at hard X-ray energies. Indeed, if a single partial coverer were adopted, the data would still prefer an intermediate column of $\sim 2.4\times10^{23}$ cm^{-2}, although the underlying spectral slope would reduce to $\Gamma \sim 1.9$ and, overall, the fit would be barely acceptable ($\chi^2_\nu \simeq 1.3$).

Except for the gap of ∼ 6–7 weeks in the observations, the comparison of EPIC/pn with HETG is definitely more informative than that with the simultaneous RGS, given the broader bandpass superposition. Focusing on the cold absorbers, both the column densities and the ionization parameters are entirely consistent. Only the discrete covering fractions are quite different, but their sum is about 75 per cent at both epochs, so that only one fourth of the intrinsic power law is not obscured by any cold gas component. As also illustrated in Fig. 3, this means that the absorption-corrected X-ray output of MR 2251−178 exceeds the observed luminosity by a factor of ∼ 3, once all the putative layers have been disentangled. We will touch again on these points in Section 4. Here we note that, in the partial covering scenario depicted so far, the apparent soft excess observed below ∼ 0.7 keV is just a fake feature imprinted on the spectrum of MR 2251−178 by the combination of warm and cold absorption effects. The other possibility is an actual softening of the primary X-ray continuum towards the lower energies.

3.2.2 Disc reflection models

Soft excesses over the extrapolation of the main power law are found almost ubiquitously among AGN with little obscuration (e.g. Porquet et al. 2004), suggesting that they may represent a genuine ingredient of the intrinsic X-ray emission. As such, this component has met over the years many alternative interpretations, still remaining largely ambiguous. One of the proposed explanations is that the host of soft X-ray fluorescent lines from the most abundant el-

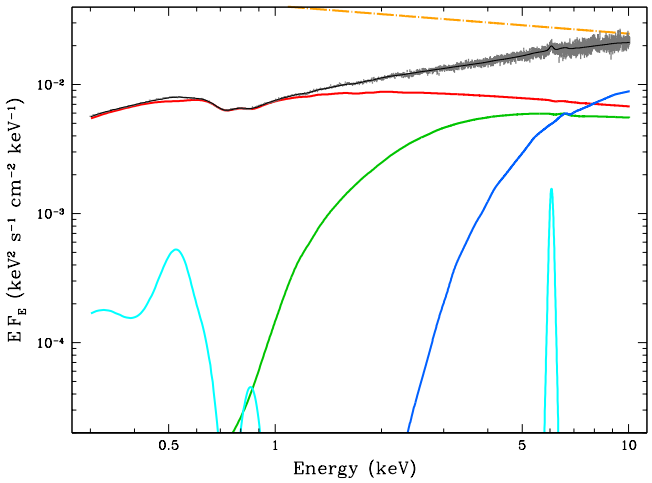

Figure 3. Illustration of the *pcovpow* model and its different spectral components (still convolved with the detector's response) against a power law with $\Gamma = 2$. Based on the amount of foreground absorption, the intrinsic continuum (shown as a dot-dashed orange line for comparison) is split into three parts, respectively transmitted through the warm absorber only (red) and through an additional cold screen with either $N_{\rm H,1} \sim 6 \times 10^{22}$ cm^{-2} (green) or $N_{\rm H,2} \sim 6.6 \times 10^{23}$ cm^{-2} (blue). The blend of soft X-ray emission lines (whose parameters were kept fixed to the RGS-inferred ones) is plotted in cyan alongside the narrow Fe Kα feature.

ements, produced in the outer layers of the accretion disc as a result of the intense X-ray illumination, are blended into a smooth pseudo-continuum due to relativistic blurring (Crummy et al. 2006). The tell-tale signature of disc reflection is usually considered the broad, skewed component of the Fe Kα emission line around 6.4 keV (e.g. Tanaka et al. 1995). This has never been reported in MR 2251−178, nor seems it to be required here at a simple visual inspection. It is well known, however, that this feature is hardly distinguishable from a continuum curvature, possibly induced by complex absorption patterns (Turner & Miller 2009), and this uncertainty works both ways.

We have therefore concentrated on the 3–10 keV band, attempting to model any iron emission in excess of the faint narrow line at ~ 6.43 keV (see Table 4). Even though the underlying power law is modified by the foreground Galactic column only, which has negligible influence on this range, all the fits are remarkably good, with $\chi^2_\nu < 1$. Switching to a broad Gaussian line delivers just a slight improvement ($\Delta\chi^2 \simeq -7.5$). We have then maintained the Kα profile unresolved, including instead a `laor` relativistic line (Laor 1991), whose shape expresses the motion of the accretion flow within the disc as a function of its inner radius (in $r_{\rm g} = GM_{\rm BH}/c^2$ units), inclination with respect to the line of sight, and emissivity index (complying with a $\epsilon \propto r^{-q}$ radial emissivity profile). As all these parameters cannot be constrained at once, we have assumed for the latter two the default values of $\theta = 30^\circ$ and $q = 3$. In this case, we achieve a $\Delta\chi^2 \simeq -41$ with the loss of three degrees of freedom, without affecting the properties of the narrow core. The inferred equivalent width of the disc line is modest (57±40 eV), and its energy of ~ 6.54 keV would imply a moderate disc ionization.

Table 4. Fit to the 3–10 keV band with a power-law continuum plus iron emission modelled as: (1) a narrow Gaussian line; (2) a broad Gaussian line, (3) a narrow Gaussian line and a `laor` disc line ($q = 3$, $\theta = 30^\circ$). E: line rest energy in keV. σ: line width in keV. EW: line equivalent width in eV. (All the other quantities are the same defined earlier in Table 3).

Model	(1)	(2)	(3)
Γ	$1.578^{+0.006}_{-0.007}$	$1.580^{+0.007}_{-0.006}$	$1.583^{+0.006}_{-0.007}$
K	0.840±0.006	0.842±0.008	0.841±0.009
$E_{\rm G}$	$6.429^{+0.016}_{-0.017}$	$6.441^{+0.021}_{-0.026}$	$6.427^{+0.019}_{-0.020}$
$\sigma_{\rm G}$	0.01(f)	$0.10^{+0.04}_{-0.03}$	0.01(f)
EW$_{\rm G}$	23±6	30±19	17±7
$E_{\rm L}$	–	–	$6.54^{+0.14}_{-0.11}$
$r_{\rm in}$	–	–	< 3.9
EW$_{\rm L}$	–	–	57±40
χ^2/ν	1165.0/1180	1157.5/1179	1124.4/1177

While this is far from being robust evidence in favour of a broad iron line, it is still worth testing a self-consistent treatment of all the reflection effects. Following some previous studies (e.g. Nardini et al. 2011), we have defined a model (tagged as *discref*) consisting of two separate reflection components arising from different locations: one is ascribed to the photoionized surface of the accretion disc, and is subject to relativistic blurring (imparted through the `kdblur` convolution kernel); the other is associated with reprocessing material at larger distance, and is expected to account for the narrow Fe Kα line. The reflection spectra have been modelled with the `xillver` tables of García et al. (2013), and are characterized by iron abundance, ionization state of the gas, and photon index of the illuminating power law (assumed to be the same of the intrinsic continuum). These add to the key blurring parameters defined above. No partial covering is included, and the soft X-ray emission lines have been initially dropped.

The *discref* model provides a broadly acceptable description of the entire 0.3–10 keV spectrum ($\chi^2/\nu \simeq 1899.5/1712$), though slightly worse than *pcovpow*. All the results are listed in Table 3. The disc component is highly significant: once deleted, it is impracticable to recover a sensible fit ($\Delta\chi^2 \sim 987$). This notwithstanding, as shown in Fig. 4, we are not witnessing a reflection-dominated spectral state. While iron abundance is suggested to be around twice solar, the disc inclination is small ($\theta \sim 25^\circ$) and the emissivity index is not so steep to entail a strongly non-isotropic X-ray illumination due to light bending (Wilkins & Fabian 2012). The disc inner radius is consistent with a Schwarzschild black hole. Accepting that the disc is not truncated off the innermost stable circular orbit, the dimensionless spin parameter $a^* = cJ/GM^2$ (where J and M are the black hole angular momentum and mass) is constrained to be < 0.65 at the 3σ level, whereas the successful application of disc reflection models usually returns rapidly spinning black holes (e.g. Walton et al. 2013; Risaliti et al. 2013). This could be due, at least in part, to the differences between the `xillver` and the `reflionx` (Ross & Fabian 2005) reflection tables at soft X-ray energies, especially for hard illuminations ($\Gamma < 2$; see García et al. 2013 for details). In any case, the reflection strength of $R \sim 1.2$ would not be compatible with an extreme gravity regime. This quantity has

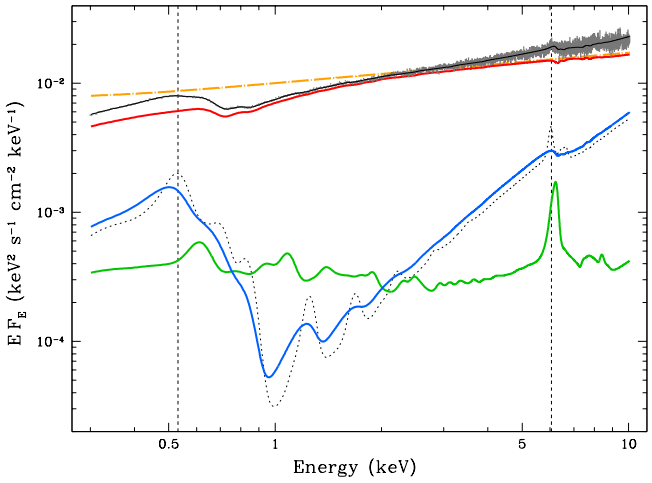

Figure 4. Same as Fig. 3 for the *discref* model. The disc component, blurred by the relativistic effects, is shown in blue, while the contribution arising from material located much farther off the illuminating source is shown in green. The dotted curve portrays the spectral shape of disc reflection before the application of any distortions, among which gravitational redshift is clearly appreciable. The vertical dashed lines mark the energies of the O VII soft emission feature and of the narrow Fe Kα core, respectively.

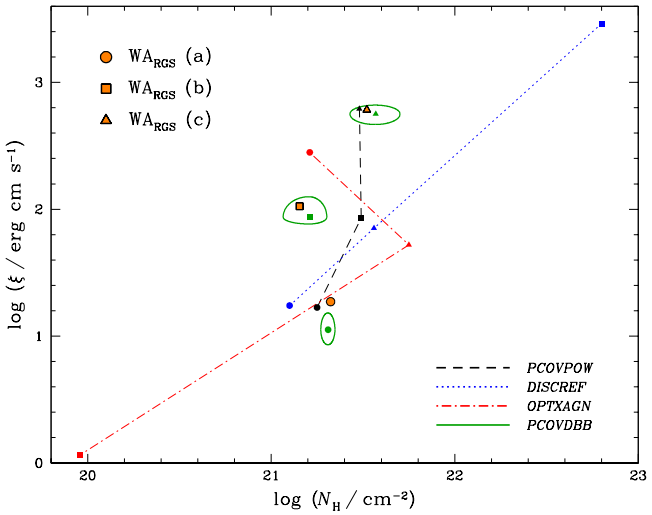

Figure 5. Location of the three warm absorbers in the N_H–ξ parameter space according to the alternative spectral models: *pcovpow* (black), *discref* (blue), and *optxagn* (red). Different symbols are used for each component: dots (a), squares (b), and triangles (c). The highlighted orange points mark the position of the RGS reference values given in Table 1. For simplicity, error ellipses are only shown for the best-fitting *pcovdbb* composite model, showing its excellent agreement with the high-resolution analysis. We remind that the identification of a given component is based on its outflow velocity.

been computed following the definition within the standard `pexrav` model (Magdziarz & Zdziarski 1995), where a value of $R = 1$ is expected in the classical limit for a plane-parallel slab subtending a solid angle of 2π at the X-ray source.

It is interesting to point out, however, that the photon index $\Gamma \simeq 1.77$ is still fairly hard, and that the ionization state of the two reflection components is somewhat in contrast with the expectations, indicating a relatively cold disc with $\log(\xi/\mathrm{erg\,cm\,s^{-1}}) \simeq 0.8$, against a rather warm distant reflector with $\log(\xi/\mathrm{erg\,cm\,s^{-1}}) \simeq 2.5$. Although the narrow K$\alpha$ core is not formally consistent with an origin from neutral gas (Table 4), here it peaks at a rest-frame energy of ~ 6.6 keV, which is definitely too high. This actually seems to replace the disc line of the phenomenological fit above, as if the smoothing imposed by the soft excess were far higher than required by the iron K band. This is a well known issue with broadband reflection models. The high ionization of the distant reflector is then likely an artefact to offset the deficiencies of the smeared component, including the poor fit to the soft X-ray emission lines, which are resolved by the gratings and have a non-relativistic widths.[3] To this spectral tweaking significantly contributes the warm absorber, whose properties are strained up to the switch between the mid- and high-ionization zones (Fig. 5). Although these two components are individually hard to constrain, freezing N_H and ξ at the fiducial values returns a $\Delta\chi^2_{N_H,\xi} \sim 199$ (Table 3). We have therefore attempted to reintroduce the soft X-ray emission-line complex, discarding the distant reflector and retaining the narrow Fe Kα feature only. The deviations of the warm absorbers are indeed reduced, and the fit improves down to $\chi^2/\nu \simeq 1874.4/1711$, yet a clear fine-tuning of the relativistic blurring is now involved ($q > 9$, $r_{in} < 1.3\,r_g$, and $\theta \sim 70°$). Hence, we did not pursue this speculation any further, sticking to *discref* in the following for discussion purposes. In summary, while we cannot exclude the presence of disc reflection, the related physical conditions are strongly model-dependent.

[3] Replacing the soft X-ray plus Fe Kα emission lines with a single `xillver` table in *pcovpow* the statistics worsens by $\Delta\chi^2 \simeq 65$. This is likely due to the scattered distribution of the reprocessing gas, as suggested by the different velocity widths of the various features (Table 2; R13).

3.2.3 Comptonization models

An alternative explanation of the soft excess is Compton up-scattering of the disc photons by an electron population with lower temperature and larger optical depth compared to the plasma in the hard X-ray corona that gives rise to the main power-law continuum (e.g. Haardt & Maraschi 1993). We have first tested this physical interpretation by applying the basic `compTT` model (Titarchuk 1994), which allowed us to mimic the effects of cold/warm Comptonization in a relatively straightforward manner through the Wien temperature of the seed photons, and the temperature and optical depth of the scattering electrons. More sophisticated models are available (Poutanen & Svensson 1996; Coppi 1999), but the choice of many geometrical and physical variables is in practice largely arbitrary, making it not possible to constrain them all simultaneously.

For consistency, both the soft excess and the hard continuum have been reproduced through Comptonized components, with an input photon temperature of 50 eV. The resulting model is referred to as *comp2tt*, and provides an equally effective fit to the data as the partial covering and disc reflection ones, with $\chi^2/\nu = 1893.5/1714$. The thermal energy of the electrons and the optical depth can be largely degenerate in Comptonization models, due to the limited

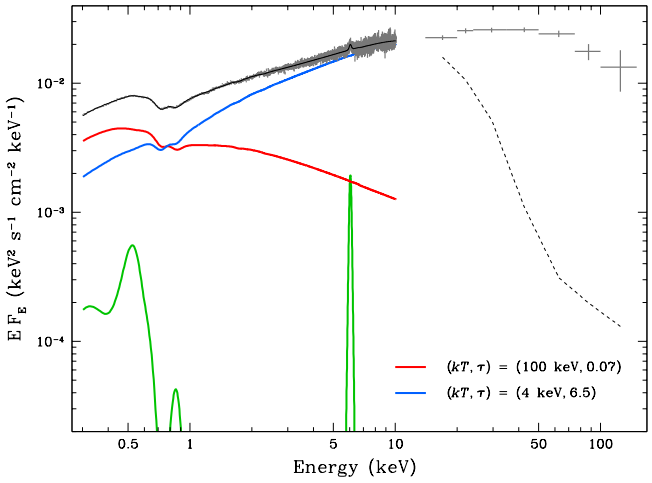

Figure 6. Spectral decomposition according to the *comp2tt* model, with the *inverted* soft/hot and hard/warm Comptonized continua plotted in red and blue, respectively (see the text for details). The emission-line spectrum is shown in green. The extrapolation towards the higher energies reveals the abrupt cut-off that characterizes this configuration. Forcing a standard behaviour (i.e. hot power-law tail versus cold soft excess), all the pure Comptonization models are moderately unsuccessful at 0.3–10 keV, making this interpretation highly problematic.

bandpass. We have then frozen the temperature of the hot Comptonizing region at $kT_e = 100$ keV, for a corresponding $\tau \sim 0.07$. Quite unexpectedly, it is the same optically thin component that becomes sharply dominating below 0.7 keV, entirely accounting for the soft excess. Indeed, this is virtually identical to a power law with $\Gamma \simeq 2.6$. The optically thick ($\tau \sim 6.5$) counterpart, instead, conforms to the curvature of the 2–10 keV spectrum with its anomalously warm temperature of 4 keV. Forcing a more realistic value of $kT_e = 0.2$ keV (see e.g. Porquet et al. 2004; Gierliński & Done 2004), the two components are reverted to their expected role, but this gives a much worse fit ($\Delta\chi^2 > 100$). Another major question raised by this model concerns the nature of the X-ray corona and its coupling with the disc, suggesting a complex structure and a high degree of inhomogeneity. In principle, though, the temperature of the cold/warm Comptonization zone could be the input for further reprocessing.

A possible solution to this coronal duality is represented by the `optxagnf` model (Done et al. 2012), in which the three separate components (thermal emission, soft excess and power-law continuum) are self-consistently powered by the energy dissipated within the accretion flow. A key parameter is the size of the corona ($r_{\rm cor}$), acting as a transitional radius beyond which the emission is characterized by the colour temperature corrected blackbody from the outer disc. Below this boundary and down to the innermost stable orbit (determined by the black hole spin), the released gravitational energy is reprocessed into either the soft excess or the hard power law through Compton upscattering (possibly taking place in the cold/warm disc atmosphere and in the proper hot corona, respectively). The power law fraction $f_{\rm pl}$ indicates the energy balance between the two components, while the total luminosity budget depends on the black hole mass (estimated to be $2.4 \times 10^8 M_\odot$ in MR 2251−178; Dunn et al. 2008), its spin, and the accretion rate. Due to a substantial degeneracy among the parameters, we have frozen $r_{\rm cor} = 10\, r_{\rm g}$, and assumed that the source radiates at 10 per cent of its Eddington luminosity, i.e. $\log(L/L_{\rm Edd}) = -1$. The outer disc radius was set to $10^5\, r_{\rm g}$.

Besides the complex continuum encompassing the contributions outlined above, this new model (dubbed as *optxagn*) consists of the usual warm absorption components and of the soft X-ray plus Fe Kα emission lines. The outcome is a slightly better fit with respect to *comp2tt* ($\chi^2/\nu = 1890.5/1714$), with a power-law photon index of $\Gamma \simeq 2.45$ (Table 5), fully consistent with the illumination required by the low-ionization warm absorption lines. Contrary to *discref*, here the central black hole is suggested to rotate quite rapidly, with $a^* \sim 0.92$. This is not to be taken at face value, as even a minor adjustment of the other quantities (e.g. doubling both $L/L_{\rm Edd}$ and $r_{\rm cor}$) leaves the goodness of fit virtually unchanged ($\Delta\chi^2 = 3.5$) without implying any spin. It is also worth noting that after thawing the Eddington ratio and the coronal radius the fit improves by $\Delta\chi^2 = -5.9$ only, delivering $\log(L/L_{\rm Edd}) \simeq -0.5$ and $r_{\rm cor} \sim 5\, r_{\rm g}$. In any case, the major issue of a twisted spectral decomposition is still present, since the temperature ($kT_e \sim 4$ keV) and optical depth ($\tau \sim 7$) of the intended soft excess strictly coincide with those of the warm/hard zone in *comp2tt*.[4] This configuration can be ultimately ruled out considering its behaviour above 10 keV, which is clarified by means of *comp2tt* in Fig. 6. Since it is driven by the 2–10 keV curvature, the optically-thick component abruptly fades at higher energies, where also its power-law-like counterpart is negligible due to its steepness. As a result, the shape of the $\sim$ 14–150 keV spectrum obtained by the Burst Alert Telescope (BAT) onboard *Swift* in the 70-month all-sky survey (December 2004–September 2010; Baumgartner et al. 2013) is completely missed.

Another severe problem with the Comptonization scenario is the loss of any agreement with the gratings on the properties of the warm absorber. Even the pivotal low-ξ component turns out to be much more ionized than expected (by a factor of $\sim$ 15; Fig. 5). If $N_{\rm H}$ and ξ are not allowed to vary from the RGS measures, the fit is not acceptable ($\chi^2_\nu \sim 1.7$ even thawing $L/L_{\rm Edd}$ and $r_{\rm cor}$). We conclude that pure Comptonization-based models (i.e. not affected by either partial covering or disc reflection) are unsuitable to describe the broadband X-ray emission of MR 2251−178, as it is not possible to reproduce both the overall curvature and the double spectral break (i.e. steep–flat–steep) at $E < 1$ keV and $E > 10$ keV (see Section 3.3).

3.2.4 Composite models

While pointing to completely different physical processes, on sheer statistical grounds all the interpretations discussed so far are almost equivalent in reproducing the 0.3–10 keV emission of MR 2251−178. The fit residuals only show limited structures (Fig. 7). The *discref* and *optxagn* models have several shortcomings, though. Taking a step further,

[4] The Compton temperature of the power-law tail is bound to 100 keV within the `optxagnf` model.

Table 5. Best-fitting parameters for the *optxagn* model. $L/L_{\rm Edd}$: Eddington ratio. a^*: dimensionless black hole spin. $r_{\rm cor}$: radius of the X-ray corona in $r_{\rm g}$. $f_{\rm pl}$: fraction of the dissipated accretion energy emitted in the hard power-law component. (See the text for details).

$\log(L/L_{\rm Edd})$	-1.0(f)	$\log N_{\rm H,a}$	$21.21^{+0.08}_{-0.09}$
a^*	$0.92^{+0.03}_{-0.02}$	$\log \xi_{\rm a}$	$2.45^{+0.08}_{-0.06}$
$r_{\rm cor}$	10(f)	$\log N_{\rm H,b}$	$19.96^{+0.31}_{-0.10}$
kT_e	$3.9^{+0.3}_{-0.2}$	$\log \xi_{\rm b}$	< 0.68
τ	$6.8^{+0.5}_{-0.4}$	$\log N_{\rm H,c}$	21.75 ± 0.03
Γ	$2.45^{+0.14}_{-0.10}$	$\log \xi_{\rm c}$	$1.72^{+0.03}_{-0.02}$
$f_{\rm pl}$	0.56 ± 0.02	$\log N_{\rm H}(z)$	$20.37^{+0.05}_{-0.03}$
$E_{\rm G}$	$6.430^{+0.017}_{-0.018}$	χ^2/ν	1890.5/1714
$\mathrm{EW_G}$	20 ± 3	$\Delta\chi^2_{N_{\rm H},\xi}$	1160

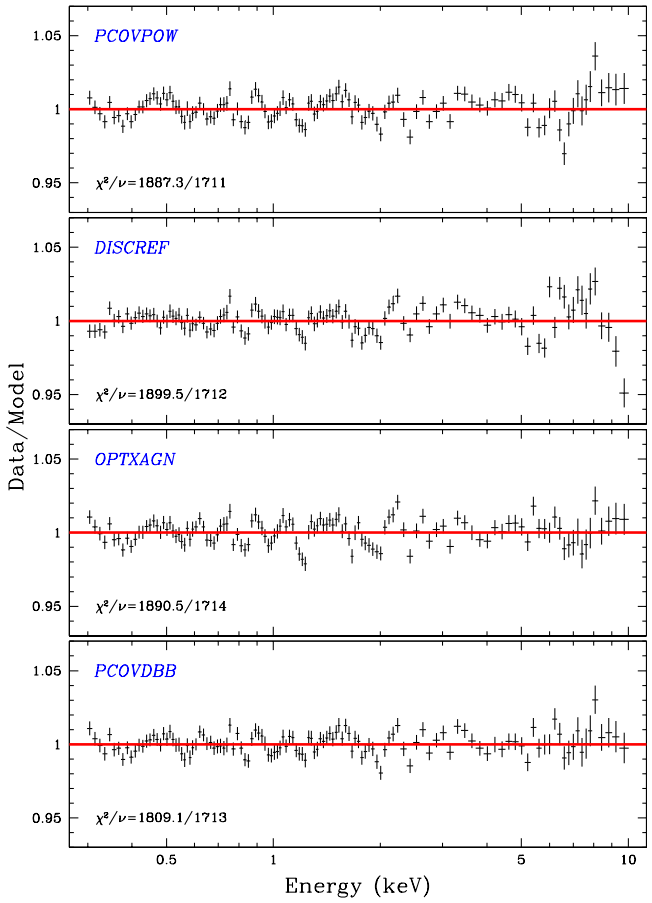

Figure 7. Residuals for the different best fits over the 0.3–10 keV energy range, plotted as data/model ratios. The spectra have been heavily rebinned in order to emphasize the main structures, especially the drop beyond ~ 9 keV in the reflection-based model (second panel from top).

we have then attempted to combine the key components of disc reflection and Comptonization with line-of-sight cold absorption, in order to investigate whether these processes are simultaneously present.

We have first introduced a single partial covering layer with ionization parameter fixed to zero in *discref*, assuming the same obscured fraction for the power-law continuum and the blurred reflection component. This model is labelled as *pcovref*, and leads to an improvement of $\Delta\chi^2 \simeq -41.8$ with the loss of one degree of freedom.[5] The full results are listed in Table 3. Since the covering fraction is fairly small, just around 0.1, this should be regarded as a refinement of *discref* rather than as a self-standing composite model. The properties of the mid- and high-ionization warm absorbers are still misreported, and the pattern in the fit residuals above 9 keV (Fig. 7) is still evident. Nevertheless, the cold-gas column of $\sim 5\times10^{22}$ cm^{-2}, which is very similar to that of the thinner layer in *pcovpow*, indicates that the existence of significant reflection from the disc is mutually exclusive with that of a gas screen much thicker than 10^{23} cm^{-2}.

Table 6. Best-fitting parameters for the *pcovdbb* model. $kT_{\rm in}$: temperature at the inner disc radius in keV. $L_{\rm bb}$: observed 0.3–2 keV soft excess flux in erg s^{-1} cm^{-2}. (Compare with Table 3).

Γ	$1.74^{+0.02}_{-0.01}$	$\log N_{\rm H,b}$	$21.21^{+0.09}_{-0.15}$
K	1.23 ± 0.03	$\log \xi_{\rm b}$	$1.94^{+0.16}_{-0.06}$
$kT_{\rm in}$	0.139 ± 0.003	$\log N_{\rm H,c}$	$21.57^{+0.13}_{-0.14}$
$\log L_{\rm bb}$	-11.41 ± 0.06	$\log \xi_{\rm c}$	$2.75^{+0.07}_{-0.08}$
$\log N_{\rm H,1}$	$23.42^{+0.04}_{-0.03}$	$\log N_{\rm H}(z)$	$20.37^{+0.04}_{-0.03}$
f_1	$0.17^{+0.02}_{-0.01}$	$\log L_{\rm int}$	44.96
$\log N_{\rm H,a}$	21.31 ± 0.04	χ^2/ν	1809.1/1713
$\log \xi_{\rm a}$	$1.05^{+0.13}_{-0.12}$	$\Delta\chi^2_{N_{\rm H},\xi}$	26.8

On the other hand, it is not straightforward to implement any partial covering within *optxagn* for normalization reasons. We have then opted for the more flexible power law plus soft excess format, modelling the latter component with a `diskbb` blackbody spectrum (e.g. Makishima et al. 1986) for simplicity.[6] We hence refer to this model as *pcovdbb*. The fit statistics undergoes a remarkable improvement down to $\chi^2/\nu \simeq 1809.1/1713$. Most importantly, this is not achieved at the expense of the warm absorption properties, whose conservation is excellent (Fig. 5). The results are listed in Table 6. Due to its temperature of $kT_{\rm in} \sim 0.14$ keV the soft excess has no contribution above 2 keV, so that any obscured blackbody emission would be completely obliterated by the column density of $N_{\rm H} \sim 3\times10^{23}$ cm^{-2} (Fig. 8). Since this component allegedly arises from the very inner regions, we expect the same covering fraction $f \sim 0.17$ of the power law to apply. As a consequence, the intrinsic luminosity of the soft excess should be corrected by a factor $(1-f)^{-1} \sim 1.2$, accounting for $\sim$ 20–25 per cent of the total output of the source at 0.3–2 keV. In general, the *pcovdbb* model appears as the most successful description of the X-ray spectrum of MR 2251−178.

3.3 Optical to X-ray spectral energy distribution

As anticipated for the unrestricted Comptonization models, a viable method to distinguish among the competing sce-

[5] The location of the remote reflector with respect to the absorber is not critical. For simplicity, this component was left unaffected. Note that, qualitatively, equivalent results are obtained if the individual emission lines are used instead.

[6] The nominal lower limit for kT_e in `compTT` is 2 keV, thus the typical temperatures of the soft X-ray excess are not sampled. Forcing this restriction, the cold Comptonization component systematically tends to a blackbody-like shape in our fits, since $\tau > 30$.

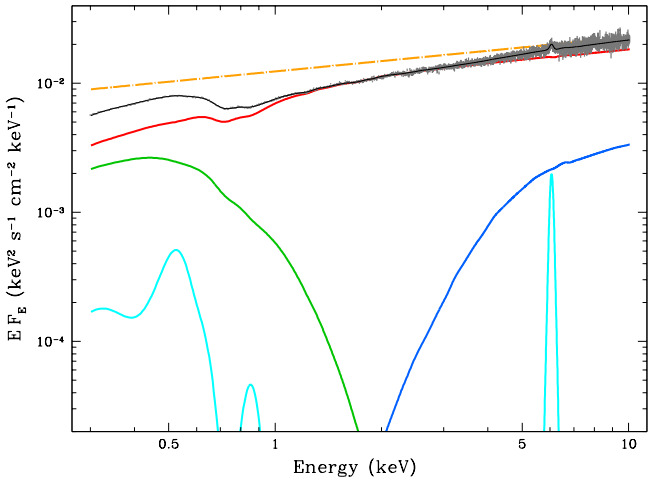

Figure 8. Same as Fig. 3 for the best-fitting *pcovdbb* model. In this scenario, the primary power-law continuum (dot-dashed orange line) is considerably flatter, and mostly transmitted through the warm absorber only (red). Just a fraction of about one sixth (blue) is obscured by an additional column of $N_{\rm H} \sim 3 \times 10^{23}$ cm^{-2}. An intrinsic soft excess (green), possibly arising as Comptonized disc emission, emerges below 2 keV. The emission-line complex is plotted in cyan.

Table 7. Key parameters of the extended fit to the 14–150 keV *Swift*/BAT spectrum. $E_{\rm C}$: exponential cutoff energy in keV. $E_{\rm F}$: e-folding energy in keV. $\mathcal{C}$: cross normalization factor.

Model	*pcovpow*	*discref*	*pcovdbb*
$E_{\rm C}$	> 70	68^{+21}_{-15}	35^{+22}_{-14}
$E_{\rm F}$	100(f)	100(f)	98^{+44}_{-51}
$\mathcal{C}$	1.22±0.06	0.58±0.02	0.90±0.05
χ^2/ν	1921.6/1716	1903.3/1717	1812.1/1717

narios is to test the models over a broader spectral range, especially at higher energies, where a diverging behaviour is most likely. In principle, the 2009 *Suzaku* spectrum analysed by Gofford et al. (2011) could be very instructive in this respect, yet the current models are too intricate for that data quality. The same *Suzaku*/PIN detection is quite noisy and provides virtually no constraints beyond ~ 30 keV. We have therefore retrieved the $\sim$ 14–150 keV 70-month *Swift*/BAT spectrum, which should be representative of the average intrinsic emission in the very hard X-ray domain as it is not affected by the column densities at issue. In terms of a simple power law, the BAT slope is $\Gamma \sim 1.95$–2.07 (with $K \sim 2.0$–3.1×10^{-2} photons keV^{-1} cm^{-2} s^{-1}; compare with Tables 3 and 6), yet some curvature is still present, as is a possible cutoff beyond $\sim$ 70–80 keV (Fig. 6; see also Orr et al. 2001). An exponential break was then adopted, parameterized through the cutoff ($E_{\rm C}$) and e-folding ($E_{\rm F}$) energies.[7]

The absorption and reflection frameworks are characterized by an opposite orientation towards the very hard X-ray spectral shape, although all the other quantities remain strictly consistent with the values obtained in the 0.3–10 keV analysis, given the low statistical weight of the BAT spectrum. Specifically, the extrapolation of the intrinsic continuum with $\Gamma \sim 2.2$ in *pcovpow* falls short across ~ 50 keV, where the curvature simulates a sort of broad, residual hump that remains unfitted. The original goodness is preserved in *discref* through a standard rollover at ~ 70 keV, yet the most effective model is confirmed to be *pcovdbb* ($\Delta\chi^2/\Delta\nu \simeq 3.0/4$), with $E_{\rm C} \sim 35$ keV and $E_{\rm F} \sim 100$ keV (Table 7). Also the cross normalization factor $\mathcal{C}$ between the EPIC/pn and BAT spectra is a valuable diagnostic. In the pure partial covering scenario we get $\mathcal{C} \sim 1.2$, meaning that during the *XMM–Newton* observation the source has to be moderately underluminous with respect to its average state. In other words, the hard X-rays are somewhat underpredicted. The contrary occurs with disc reflection, for which $\mathcal{C} \sim 0.6$, while in the composite *pcovdbb* case the match is virtually optimal, with $\mathcal{C} \simeq 0.90(\pm 0.05)$. Such incongruences are potentially revealing, and are inherent to the models themselves. In fact, while any absorption effect rapidly decreases with energy, the reflection contribution grows, and the presence of a strong reflection component on top of a flatter $\Gamma \sim 1.8$ keeps the flux level above 10 keV significantly higher. The implications will be further discussed in the next Section.

Switching to the low energy side, it is worth considering the source flux in the six *XMM–Newton*/OM filters. It is quite striking that the extrapolation of the *Swift*/BAT spectral shape generally overlaps with the optical points, with a slope just slightly steeper than $\Gamma \sim 2$. The variability of MR 2251−178 in the optical and X-ray bands is known to be very well correlated, with a mutual delay consistent with zero and anyway not larger than four days (Arévalo et al. 2008), i.e. less than the span of this long-look observation. However, it is unlikely for a single continuum component to extend across nearly five decades in energy, with just the partial covering absorption effects producing an apparent broad trough at $\sim$ 1–10 keV. Like the high-energy cutoff in the primary X-ray power law can be naturally related to the temperature of the relativistic electrons in the corona, a similar drop in response to the temperature of the seed photons from the disc must stand somewhere in the UV. With the central black hole accreting at a $\sim$ 0.1–0.5 fraction of the Eddington rate, the inner disc temperature in MR 2251−178 is predicted to lie in the range from $\sim$ 10 to 50 eV, irrespective of the exact spin (e.g. Peterson 1997). No substantial power-law contribution should then leak down to the OM bands. In any case, the optical and X-ray sources are tightly connected, and the former can be almost certainly identified with the accretion disc.

The only model that intrinsically includes the disc thermal emission is *optxagn*. Neglecting the extremely poor fit statistics at 0.3–10 keV and any discrepancy with the BAT spectrum, once informed with the results of *pcovdbb* on e.g. kT and Γ, *optxagn* yields a very smooth connection to the OM fluxes, with all the six points falling within 30 per cent of the extrapolation from the X-ray band for a range of sensible values of both the Eddington ratio and the coronal radius. It should be noted that departures from the adopted Galactic extinction law might be involved, as well as some extra reddening local to the source, possibly subject to the anomalous dust-to-gas ratios commonly found among AGN

[7] The multiplicative high-energy cutoff `highecut` in XSPEC is defined as $\exp[(E_{\rm C}-E)/E_{\rm F}]$ for $E > E_{\rm C}$, while the data below $E_{\rm C}$ are not modified.

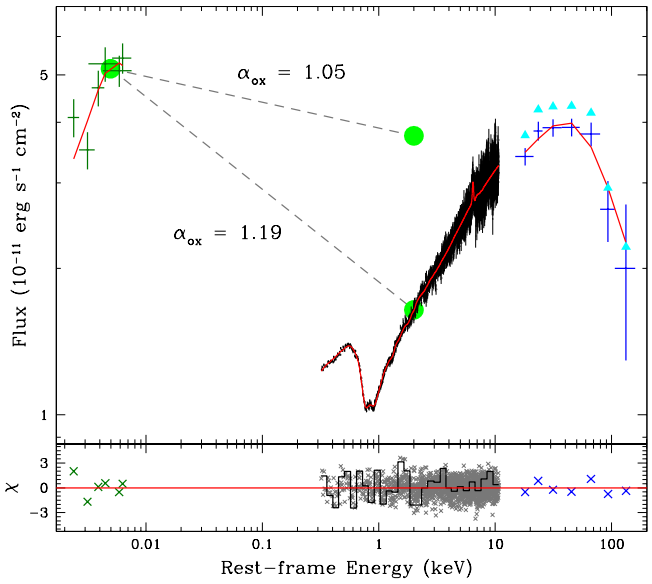

Figure 9. Top panel: optical to hard X-ray spectral energy distribution of MR 2251−178, plotted in *fluxed* units (i.e. νf_ν) and obtained as a ratio over a power law with $\Gamma = 2$ (note that this is still an approximation; see the Appendix A in Vaughan et al. 2011 for a thorough discussion on the visualization of *true* X-ray spectra). The red solid curve traces the best-fitting extended *pcovdbb* model, which includes a second, low-temperature disc component and a high-energy cutoff. The simultaneous *XMM–Newton* OM and EPIC/pn data (corrected for Galactic extinction and absorption) are combined with the *Swift*/BAT spectrum averaged over 70 months (blue crosses; the cyan points are shifted upwards by $\sim$ 10 per cent according to the cross normalization factor, although it is most likely that the pair of *XMM–Newton* spectra are slightly brighter than usual). The possible range for the optical to X-ray spectral index (no absorption correction and double partial covering case) is also shown. Bottom panel: residuals in units of σ. The error bars (of size 1) have been omitted.

(e.g. Maiolino et al. 2001). Moreover, the OM fluxes could contain some contribution from the strong emission lines revealed by the *HST* UV spectrum (Monier et al. 2001), in particular Mg II in UVW1 and C III] in UVW2. None the less, the observed correspondence suggests that the basic geometrical and physical assumptions underlying the `optxagnf` Comptonization picture (Done et al. 2012) are relevant to MR 2251−178, at least qualitatively. The unprocessed disc component has to be included in all our other models as a separate multi-temperature blackbody. Being constrained over the OM range only, the peak temperature is $kT \sim 2$–3 eV, and the luminosity is $L_{\rm disc} \sim 10^{45}$ erg s^{-1}. We consider this a conservative limit for the thermal emission from the outer disc. The optical to hard X-ray spectral energy distribution (SED) of MR 2251−178 is shown in Fig. 9, together with its best-fitting *pcovdbb* description.

4 DISCUSSION

The 2011 *XMM–Newton* observation supplied the highest-quality X-ray spectrum of MR 2251−178 to date, with over 5 million net counts over the 0.3–10 keV band. This notwithstanding, based on the EPIC/pn analysis alone the origin of the intrinsic X-ray continuum would remain somewhat unclear, as partial covering absorption, ionized reflection, and Comptonized disc emission models cannot be statistically discriminated at CCD resolution. The availability of exquisite high-resolution data offers a straightforward way to test the soundness of the different fits, in which the column densities and ionization parameters of the warm absorption components have been allowed to vary with respect to the reference values of Table 1. Indeed, while various warm absorber configurations are still acceptable for the 0.3–10 keV continuum shape, it is evident from Fig. 5 that in some cases the combined shifts in both $N_{\rm H}$ and ξ lead to a complete displacement of a given component within the parameter space. To a lesser extent, this is also true for the finest grid, which is the best-constrained in the broadband analysis due to its low ionization (e.g. Table 3). The quantity $\Delta\chi^2_{N_{\rm H},\xi}$ has been used as a gauge of how much the warm absorption properties are distorted to minimize the fit statistics of each model. The deviations are largest in reflection-based models, which show strong residuals (mainly corresponding to the O VII emission line) when superimposed on the RGS spectra.[8] Not surprisingly, *pcovpow* is instead nearly consistent with R13, where an equivalent partially covered continuum was adopted. Yet, the closest agreement is delivered by *pcovdbb*, with $\Delta\chi^2_{N_{\rm H},\xi} \sim 27$ (Table 6). Indeed, in trying to fit the EPIC/pn and RGS spectra simultaneously, *pcovpow* and *pcovdbb* turn out to be equally effective.

As already mentioned, another useful diagnostic is the scale factor between the EPIC/pn and BAT spectra, especially because of the opposite trend entailed by the *pcovpow* and *discref* models. For ease of comparison, we have collected the about 40 measurements of the 2–10 keV flux obtained by ten X-ray observatories over more than three decades. The lowest and highest states correspond to the 1989 *Ginga* observation (Mineo & Stewart 1993) and to the first 1993 *ASCA* snapshot (Kaspi et al. 2004), respectively at ~ 1.7 and 5.2×10^{-11} erg s^{-1} cm^{-2}. The mean/median intensity is ~ 3.2–3.3×10^{-11} erg s^{-1} cm^{-2}, suggesting that the 2011 *XMM–Newton* campaign caught the source in a relatively bright phase, arguably $\sim$ 25–30 per cent above the average. Qualitatively, this would disfavour the pure partial covering picture, but it is not yet a conclusive hint in any direction for several reasons. The magnitude of the cross normalization actually casts serious doubts also on *discref*, whose application to the 2009 *Suzaku* data set confirms that the sizable offset between the 0.6–10 and 15–50 keV spectra is not related to different flux states. The small value of $\mathcal{C} \sim 0.6$ and the cutoff at ~ 70 keV would then compensate for the obvious absence of a prominent Compton hump, which is perhaps related also to the clear pattern in the fit residuals starting above 9 keV (Fig. 7).

On the other hand, cold absorption effects can easily halve the 2–10 keV emission, artificially expanding the scope of the intrinsic X-ray variability;[9] the source might simply look fainter because it is more obscured. In this view, even a

[8] We also emphasize that misread mid- and high-ionization zones would heavily affect the fit to the HETG spectra.
[9] Adopting a conservative binning of $\sim$ 3–4 months to obtain similar error bars on each point, the 70-month *Swift*/BAT light curve shows peak-to-peak variations by a factor of ~ 2.5.

cross normalization slightly larger than one could be broadly consistent with the observational history of MR 2251−178, also given that $\mathcal{C}$ strongly depends on the actual photon index. Moreover, in the regular monitoring by *RXTE* discussed in Arevalo et al. (2008), consisting of over 200 snapshots in 2.5 years with 1 ks exposure each, the inferred 2–10 keV flux covers the ~ 2.8–7.3×10^{-11} erg s^{-1} cm^{-2} range. Disregarding any possible systematics in the latter estimates, their average value of 5×10^{-11} erg s^{-1} cm^{-2} is about 20 per cent larger than the flux recorded in the *XMM–Newton* observation, in agreement with the extrapolation to the *Swift*/BAT spectrum of *pcovpow*, which anyway returns a very poor fit around 50 keV. As a consequence, the composite model *pcovdbb* is definitely preferred. An accurate, simultaneous broadband analysis, which has now become feasible at $\sim$ 3–80 keV thanks to *NuSTAR* (Harrison et al. 2013), is clearly needed to shed new light on the nature of the high-energy emission of MR 2251−178, although the soft X-rays cannot be neglected to properly constrain the warm absorber and the putative soft excess.

The global curvature is undoubtedly the most puzzling feature of the broadband X-ray continuum in this source, with its strikingly different slopes below and above 10 keV. A similar behaviour has been observed in a completely different object, the dwarf Seyfert galaxy NGC 4395, known to host the least massive black hole among AGN ($M_{\rm BH} \sim 10^5 M_{\odot}$; Peterson et al. 2005). Its 2–10 keV spectral shape is extraordinarily flat, characterized by a photon index that can be as low as ~ 0.6 (Moran et al. 2005), yet turning into the typical $\Gamma \sim 2$ of unobscured AGN at higher energies. NGC 4395 actually undergoes dramatic spectral variability over timescales of a few ks, which can be ascribed to a complex system of cold absorbers with column densities of $\sim 10^{22}$–10^{23} cm^{-2}, crossing the line of sight to the primary source (Nardini & Risaliti 2011). It is then possible that in MR 2251−178 the observed 2–10 keV continuum is misleading, not being representative of the intrinsic emission without a correct modelling of the absorption effects. Indeed, such a hard slope poses an issue with the depth of the inner-shell lines in the low-ionization warm absorber, which call for a soft $\Gamma \sim 2.5$ illumination. Overall, the grating analysis suggests a break in the input photoionizing spectrum, with a sort of intrinsic soft excess converting into a much flatter power law than typically found in radio-quiet quasars.

Following R13, who suggest an association with the same BLR clouds responsible for the soft X-ray emission lines, we assume that the partial-covering gas is more internal than the pc-scale warm absorber, and approximate the radiation impinging on the latter as a broken power law in order to assess its crude outline. Within *pcovpow*, the soft photon index is bound to the $\Gamma \sim 2.2$ of the unabsorbed continuum, which is possibly not steep enough to comply with the prescriptions from the warm absorption lines. The extra blackbody-like component included in the *pcovdbb* model results in a broadly acceptable effective slope of $\Gamma \sim 2.3$ below the break energy of ~ 1.2 keV. The implied temperature of ~ 0.14 keV is at least three times larger than that expected in MR 2251−178 for a standard thin accretion disc, but it is commensurate with the typical values recorded for the soft X-ray excess in AGN (e.g. Jin et al. 2012), whose origin is still essentially unknown. Despite these uncertainties, the combination of cold absorption in the form of partial covering and some kind of Compton reprocessing stands as the most convincing interpretation on the whole, also conceding that the Comptonization conjecture lends weight to the tight connection between the accretion disc and the X-ray corona (Arevalo et al. 2008).

Given that the X-ray source in AGN is presumed to be extremely compact (a few tens of gravitational radii at most), partial covering can be only envisaged in a dynamical context; in other words, it has to occur at BLR scales. It is easy to show, in fact, that if no changes in the covering factor are perceived over several years the putative absorber must be located at least a few pc away from the emitting region, and be much larger of it. Under these circumstances, any partial covering configuration is highly unlikely. Concerning MR 2251−178, the lack of any appreciable changes other than the slow decline in the overall flux intensity during the *XMM–Newton* long look is not particularly worrying given the large mass of the central black hole. The relevant timescale to the variations of the intrinsic X-ray emission, for instance, is the light-crossing time, which is $\sim$ 12 ks assuming that the source is spherical and has a diameter of $10\,r_{\rm g}$ (compare with Fig. 1). On the other hand, within an eclipsing cloud scenario (e.g. NGC 1365; Risaliti et al. 2007), the occultation time by a single gaseous clump with identical size and shape to the X-ray source in Keplerian motion at a distance of $10^4\,r_{\rm g}$ would be nearly 2 weeks,[10] against the 5.5 days of elapsed time in present observation. By using the recent $R_{\rm BLR}$–$\lambda L_{\lambda}(5100\,\text{Å})$ relationship from Bentz et al. (2013) and the average 5100 Å luminosity from Lira et al. (2011), we indeed obtain a BLR radius of about 75 light days, i.e. $5.5 \times 10^3\,r_{\rm g}$. Notably, as also reported in R13, there are hints of some change in the covering fractions between the *XMM–Newton* and *Chandra* campaigns, separated by just a few weeks.

The partial covering interpretation for the X-ray spectra of AGN thus relies on the identification of rapid spectral variability. Keeping in mind the expanded timescale, the long look of MR 2251−178 is equivalent to the shorter snapshots of NGC 4395, which sampled a single state of the source. In this framework, we can draw similar speculations on the structure of the cold X-ray absorber, holding for both *pcovpow* and *pcovdbb*. Two distinct components emerge from the pure partial covering fit. In a stratified circumnuclear medium, the possibility that two *clouds* belonging to detached layers simultaneously cover different sectors of the X-ray source is rather contrived. In principle, the disparity of about one order of magnitude between the column densities involved would allow for projection effects, with the two components partially on top of each other. The assessed covering fraction $f_1 \simeq 0.23$ would be simply a lower limit to the effective one. Yet the fact that both $N_{\rm H,1}$ and $N_{\rm H,2}$ are very well constrained, and in particular that the uncertainty on $N_{\rm H,2}$ is only $\sim 0.5\,N_{\rm H,1}$ (at the 90 per cent confidence level), seems to rule out this solution. On the contrary, a single absorber can meet the fit conditions if bearing sharp density gradients and/or irregular geometry. Indeed, it has been recently suggested that the eclipsing BLR clouds might actually have a comet-like structure, with a dense head and a tenuous tail (Maiolino

[10] It is 30 minutes in NGC 4395 under the same assumptions.

et al. 2010; Risaliti et al. 2011). Such blobs could have a lifetime of several months at most, implying that this BLR component must be continuously replenished. It is therefore a matter of duty cycle and likelihood for a gas clump to pass in front of the X-ray source. The transit of a single cloud, further supported by the robustness of the *pcovdbb* picture, is ultimately the most reliable scenario in this sense. Limited to the column density changes of the warm absorber, the presence of material moving in and out the line of sight had already been invoked (e.g. Orr et al. 2001; Kaspi et al. 2004). This bulk motion might exist throughout the spatial scales. The spectral variability aspects are then crucial for any of the physical models examined here, and will be investigated in detail in a subsequent paper (Porquet et al., in preparation) considering all the highest-quality recent and archival observations of MR 2251−178.

Summarizing, our analysis still leaves some open issues. However, irrespective of the real nature of its X-ray emission and of the amount of absorbing gas along the line of sight, MR 2251−178 is confirmed to boast one of the largest X-ray to optical luminosity ratios among radio-quiet quasars. This is clearly pointed out by its $\alpha_{\rm ox}$ spectral index.[11] Without applying any correction, the observed $\alpha_{\rm ox} \simeq 1.19$ extracted from the broadband SED of Fig. 9 is already much lower than the mean value for X-ray selected AGN, i.e. $\overline{\alpha_{\rm ox}} \simeq 1.37$ (with a 1σ dispersion of 0.18; Lusso et al. 2010). In the dual partial covering case, the rest-frame brightness at 2 keV has to be revised upwards by a factor of $\sim$ 2.3, delivering an even more exceptional optical to X-ray spectral index of 1.05. This does not heavily impact the bolometric output of MR 2251−178 though, once the correlation between $\alpha_{\rm ox}$ and the 2–10 keV to bolometric correction ($k_{\rm bol}$) is taken into account. We obtain that $k_{\rm bol} \approx 7$–12 (e.g. Lusso et al. 2010; Marchese et al. 2012), for a total luminosity $L_{\rm bol}$ of ~ 5–7×10^{45} erg s^{-1}, which is $\sim$ 15–25 per cent of the source Eddington luminosity and is just above the UV-based estimate (Dunn et al. 2008). In the light of these outstanding properties, including the possible massive disc outflow (Gibson et al. 2005; Gofford et al. 2011), unveiling the X-ray emission mechanism and its coupling with the absorbing/reprocessing gas would have far-reaching implications for the quasar radiative and mechanical feedback on the surrounding environment and all the related fields.

5 SUMMARY AND CONCLUSIONS

Based on a recent *XMM–Newton* long-look observation with $\sim$ 270 ks of net exposure, we have reported on the 0.3–10 keV EPIC/pn spectral analysis of MR 2251−178, one of the brightest radio-quiet quasars in the local Universe. Following a companion paper dedicated to the study of the high-resolution grating spectra and of the physical properties of the complex warm absorber, here we have focused on the nature of the intrinsic X-ray emission. The broadband X-ray continuum of MR 2251−178 is known to exhibit substantial curvature up to $\sim$ 100 keV, where a possible cutoff is also present. Together with the apparent soft excess below 0.7 keV and the warm absorption trough at $\sim$ 1–2 keV, this gives rise to a peculiar steep–flat–steep spectral shape, which has been inspected within the frameworks of partial covering absorption, ionized reflection, and Comptonized disc emission.

As their application turns out to be nearly statistically equivalent over the 0.3–10 keV band, all these models have also been compared with the coeval OM photometric data and the $\sim$ 14–150 keV *Swift*/BAT spectrum, averaged over 70 months. Assuming no cross normalization, the entire SED shows that the optical and hard X-ray fluxes lie at almost the same level in νf_ν units. Indeed, the optical to X-ray spectral index is extremely small ($\alpha_{\rm ox} < 1.2$), irrespective of the exact absorption correction. The corresponding bolometric output of MR 2251−178 is estimated to be $L_{\rm bol} \sim 5$–7×10^{45} erg s^{-1}, i.e. $\sim$ 15–25 per cent of the source Eddington luminosity.

None of the alternative interpretations taken into account in this work are conclusive by themselves, displaying both strengths and limitations at the same time, which can be summarized as follows:

1) The pure partial covering scenario reveals two distinct low-ionization components with columns of 0.6 and 6.6×10^{23} cm^{-2}, eclipsing a fraction of $\sim$ 0.23 and 0.49 of the X-ray source, respectively. We argue that these absorbers are located at BLR scales, but are unlikely to belong to different layers. Density gradients might be entailed, pointing to a single clump of gas with a dense core and a lighter halo. The intrinsic photon index $\Gamma \sim 2.2$ is close to what is required by the photoionization models of the warm absorber, but still somewhat lower; even so, excess curvature is left at hard X-rays around 50 keV.

2) At EPIC/pn resolution, X-ray reflection provides a reasonable fit without implying any extreme gravity regime. The blurred disc component, however, is unusually cold, and $\sim$ 50 times less ionized than its distant counterpart. This is possibly an artefact to compensate for the inadequate results with the soft X-ray emission lines (resolved by the gratings), and also leads to a misrepresentation of the warm absorption properties (for which the illumination is anyway flat). The degree of smoothing appears too large for the iron K band, and a clear pattern is found in the residuals above 9 keV. Moreover, the BAT spectrum is largely overpredicted.

3) The optically-thick/thin Comptonization of thermal photons from the inner disc into both the soft excess and the hard power law, with the outer regions emitting as a colour temperature corrected blackbody, is established as the most obvious connection between the optical and X-ray bands. Nevertheless, in spite of the remarkably good extrapolation to the OM data and of the ample leverage on the physical parameters, a basic self-consistent model either fails to reproduce the 0.3–10 keV features or invariably plummets too quickly at higher energies. Any agreement is lost on the three warm absorption components.

A composite model allows us to successfully overcome most of the above shortcomings. While reflection from the accretion flow and/or the ambient material might still be involved to a certain extent, in the preferred picture the hard power-law continuum ($\Gamma \sim 1.75$) steepens below $\sim$ 1 keV into a soft excess with $kT \sim 0.14$ keV, whose origin remains unclear although it can be tentatively associated with Comptonization in the disc atmosphere. A single cloud

[11] The optical/UV to X-ray spectral index is generally defined as $\alpha_{\rm ox} = -0.384 \log (L_{2\,\rm keV}/L_{2500\,\text{Å}})$. Note that $\alpha_{\rm ox} = 1$ for a flat SED (in νf_ν).

with $N_{\rm H} \sim 3 \times 10^{23}$ cm^{-2} is present along the line of sight, covering about one sixth of the X-ray source.

In conclusion, the X-ray observations of MR 2251−178 brought to light a complex and stratified environment close to the central source, which deeply transforms the shape of the intrinsic X-ray spectrum. Our study suggests that only a combination of time variability analysis, simultaneous broadband coverage and high spectral resolution can help disentangling the effects of the different physical processes responsible for the observed X-ray emission of AGN.

ACKNOWLEDGMENTS

The authors are grateful to the referee, Chris Done, for helpful comments that significantly improved the clarity of this paper. EN thanks Javier García for useful discussion on the reflection strength in his `xillver` table models. EN, JNR and JG acknowledge the financial support provided by STFC. JNR was also supported by *Chandra* grant number GO1-12143X. DP acknowledges financial support from the French GDR PCHE. This work is based on observations obtained with *XMM–Newton*, an ESA science mission with instruments and contributions directly funded by ESA member states and NASA.

REFERENCES

Arévalo P., Uttley P., Kaspi S., Breedt E., Lira P., McHardy I. M., 2008, MNRAS, 389, 1479
Baumgartner W. H., Tueller J., Markwardt C. B., Skinner G. K., Barthelmy S., Mushotzky R. F., Evans P. A., Gehrels N., 2013, ApJS, 207, 19
Behar E., Sako M., Kahn S. M., 2001, ApJ, 563, 497
Bentz M. C., et al., 2013, ApJ, 767, 149
Bergeron J., Dennefeld M., Boksenberg A., Tarenghi M., 1983, MNRAS, 202, 125
Canizares C. R., McClintock J. E., Ricker G. R., 1978, ApJ, 226, L1
Cardelli J. A., Clayton G. C., Mathis J. S., 1989, ApJ, 345, 245
Cooke B. A., et al., 1978, MNRAS, 182, 489
Coppi P. S., 1999, in Poutanen J., Svensson R., eds, ASP Conf. Ser. Vol. 161, High Energy Processes in Accreting Black Holes. Astron. Soc. Pac., San Francisco, p. 375
Crummy J., Fabian A. C., Gallo L., Ross R. R., 2006, MNRAS, 365, 1067
Done C., Davis S. W., Jin C., Blaes O., Ward M., 2012, MNRAS, 420, 1848
Dunn J. P., Crenshaw D. M., Kraemer S. B., Trippe M. L., 2008, AJ, 136, 1201
Ganguly R., Charlton J. C., Eracleous M., 2001, ApJ, 556, L7
García J., Dauser T., Reynolds C. S., Kallman T. R., McClintock J. E., Wilms J., Eikmann W., 2013, ApJ, 768, 146
Gibson R. R., Marshall H. L., Canizares C. R., Lee J. C., 2005, ApJ, 627, 83
Gierliński M., Done C., 2004, MNRAS, 349, L7
Gofford J., et al., 2011, MNRAS, 414, 3307
Haardt F., Maraschi L., 1993, ApJ, 413, 507
Halpern J. P., 1984, ApJ, 281, 90
Harrison F. A., et al., 2013, ApJ, 770, 103
Hinshaw G., et al., 2013, ApJS, 208, 19
Jin C., Ward M., Done C., Gelbord J., 2012, MNRAS, 420, 1825
Kalberla P. M. W., Burton W. B., Hartmann D., Arnal E. M., Bajaja E., Morras R., Pöppel W. G. L., 2005, A&A, 440, 775
Kallman T., Bautista M., 2001, ApJS, 133, 221
Kaspi S., Netzer H., Chelouche D., George I. M., Nandra K., Turner T. J., 2004, ApJ, 611, 68
Kreimeyer K., Veilleux S., 2013, ApJ, 772, L11
Lira P., Arévalo P., Uttley P., McHardy I., Breedt E., 2011, MNRAS, 415, 1290
Lusso E., et al., 2010, A&A, 512, A34
Macchetto F., Colina L., Golombek D., Perryman M. A. C., di Serego Alighieri S., 1990, ApJ, 356, 389
Magdziarz P., Zdziarski A. A., 1995, MNRAS, 273, 837
Maiolino R., Marconi A., Salvati M., Risaliti G., Severgnini P., Oliva E., La Franca F., Vanzi L., 2001, A&A, 365, 28
Maiolino R., et al., 2010, A&A, 517, A47
Makishima K., Maejima Y., Mitsuda K., Bradt H. V., Remillard R. A., Tuohy I. R., Hoshi R., Nakagawa M., 1986, ApJ, 308, 635
Marchese E., Della Ceca R., Caccianiga A., Severgnini P., Corral A., Fanali R., 2012, A&A, 539, A48
Monier E. M., Mathur S., Wilkes B., Elvis M., 2001, ApJ, 559, 675
Moran E. C., Eracleous M., Leighly K. M., Chartas G., Filippenko A. V., Ho L. C., Blanco P. R., 2005, AJ, 129, 2108
Nardini E., Risaliti G., 2011, MNRAS, 417, 2571
Nardini E., Fabian A. C., Reis R. C., Walton D. J., 2011, MNRAS, 410, 1251
Orr A., Barr P., Guainazzi M., Parmar A. N., Young A. J., 2001, A&A, 376, 413
Pan H. C., Stewart G. C., Pounds K. A., 1990, MNRAS, 242, 177
Peterson B. M., et al., 2005, ApJ, 632, 799
Phillips M. M., 1980, ApJ, 236, L45
Piconcelli E., Jimenez-Bailón E., Guainazzi M., Schartel N., Rodríguez-Pascual P. M., Santos-Lleó M., 2005, A&A, 432, 15
Porquet D., Reeves J. N., O'Brien P., Brinkmann W., 2004, A&A, 422, 85
Poutanen J., Svensson R., 1996, ApJ, 470, 249
Reeves J. N., Porquet D., Braito V., Gofford J., Nardini E., Turner T. J., Crenshaw D. M., Kraemer S. B., 2013, ApJ, 776, 99 (R13)
Ricker G. R., Clark G. W., Doxsey R. E., Dower R. G., Jernigan J. G., Delvaille J. P., MacAlpine G. M., Hjellming R. M., 1978, Natur, 271, 35
Risaliti G., Elvis M., Fabbiano G., Baldi A., Zezas A., Salvati M., 2007, ApJ, 659, L111
Risaliti G., Nardini E., Salvati M., Elvis M., Fabbiano G., Maiolino R., Pietrini P., Torricelli-Ciamponi G., 2011, MNRAS, 410, 1027
Risaliti G., et al., 2013, Natur, 494, 449
Ross R. R., Fabian A. C., 2005, MNRAS, 358, 211
Schlegel D. J., Finkbeiner D. P., Davis M., 1998, ApJ, 500, 525
Scott A. E., Stewart G. C., Mateos S., Alexander D. M., Hutton S., Ward M. J., 2011, MNRAS, 417, 992
Shopbell P. L., Veilleux S., Bland-Hawthorn J., 1999, ApJ, 524, L83
Tanaka Y., et al., 1995, Natur, 375, 659
Tarter C. B., Tucker W. H., Salpeter E. E., 1969, ApJ, 156, 943
Titarchuk L., 1994, ApJ, 434, 570
Turner T. J., Miller L., 2009, A&ARv, 17, 47
Vaughan S., Uttley P., Pounds K. A., Nandra K., Strohmayer T. E., 2011, MNRAS, 413, 2489
Walton D. J., Nardini E., Fabian A. C., Gallo L. C., Reis R. C., 2013, MNRAS, 428, 2901
Wilkins D. R., Fabian A. C., 2012, MNRAS, 424, 1284
Wilms J., Allen A., McCray R., 2000, ApJ, 542, 914